数理解析研究所講究録
1051 巻 1998 年 166-179

Chaotic Motion of Fluid Particles around a Rotating Elliptic Vortex

Faculty of Eng. Kyoto Univ. Akihiko Kawakami 川上 晶彦
Faculty of Eng. Kyoto Univ. Mitsuaki Funakoshi 船越 満明

1 Introduction

It is widely known that for an inviscid fluid an elliptical region with uniform vorticity, the Kirchhoff elliptic vortex, rotates at a constant angular velocity without changing its shape(Lamb 1957). The motion of a vortex region with uniform vorticity in a linear shear flow was investigated by Moore & Saffman(1971) and Kida(1981). Moore & Saffman(1971) obtained steady elliptic vortex and examined its stability. Kida(1981) showed that an initially elliptic vortex region in a linear shear flow remains elliptic but changes its aspect ratio and angular velocity. He also derived the evolution equations for the aspect ratio and the orientation of the ellipse. By analysing these equations, he showed that the elliptic vortex may rotate, nutate, or be elongated.

Polvani & Wisdom(1990) and Dahleh(1992) numerically investigated the motion of fluid particles around a rotating elliptic vortex in a linear shear flow, as an example of the Lagrangian chaos for a two-dimensional time-periodic flow. Polvani & Wisdom(1990) found that there exist chaotic regions surrounding the vortex even for small shear and that a fluid particle can eventually escape from the vicinity of the rotating vortex for a certain value of the shear. They also mentioned that the chaotic region appears first around the heteroclinic orbits connecting the hyperbolic fixed points of the flow field around the Kirchhoff elliptic vortex. They, however, did not confirm the appearance of the chaos analytically. Dahleh(1992) examined the spatial variability that is characterized by the separation rate of nearby particles in the chaotic region using the finite-time spreading rate and showed that particles passing near a stagnation point of the flow have a high spreading rate.

In the present paper, we study in more detail the motion of fluid particles in the same flow as Polvani & Wisdom(1990) and Dahleh(1992) used. Our purpose is to examine the dependence of the chaotic motion of fluid particles around a rotating elliptic vortex on the rate of the strain s of the external flow and on the initial aspect ratio of the ellipse. Particularly, it is aimed to confirm analytically the appearance of chaos for small s using a perturbation method. We also aim at examining the dependence of the escape motion of fluid particles on their initial positions for relatively large s.

2 Elliptic vortex in a linear shear flow

2.1 Motion of an elliptic vortex

We consider the two-dimensional motion of an elliptic vortex in a linear shear flow of an inviscid incompressible fluid. The center of this elliptic vortex with uniform vorticity ω

is located at $(x, y) = (0, 0)$, where (x, y) is two-dimensional Cartesian coordinates. The stream function of the external shear flow is given by

$$\psi_e = -\frac{1}{4}(\gamma + s)x^2 - \frac{1}{4}(\gamma - s)y^2, \tag{1}$$

where γ is vorticity and s is the rate of strain.

It was shown by Kida(1981) that the vortex region remains elliptic in this external flow and that the time evolution of the shape of this vortex region is governed by

$$\begin{cases} \dot{r} &= -sr\sin 2\theta, \\ \dot{\theta} &= \dfrac{r\omega}{(r+1)^2} + \dfrac{1}{2}\left(s\dfrac{1+r^2}{1-r^2}\cos 2\theta + \gamma\right), \end{cases} \tag{2}$$

where r is the aspect ratio and θ is the angle between the major axis and the x axis. The dot denotes the differentiation with respect to the time t. The relation

$$\cos 2\theta = \frac{2\omega}{s}\left(\frac{r}{r^2-1}\log\frac{(r+1)^2}{4pr} + \frac{\gamma}{2\omega}\frac{(r-1)}{(r+1)}\right) \equiv \frac{2\omega}{s}g(r;\gamma,\omega,p), \tag{3}$$

is obtained from Eq.(2), where p is a constant determined by the initial values of r and θ. Therefore, (r, θ) evolves along a curve specified by Eq.(3).

Since $-1 \leqq \cos 2\theta \leqq 1$, only the r-dependence of g within the range $-s/2\omega \leqq g \leqq s/2\omega$ is relevant. Kida(1981) showed that the motion of the vortex is classified into three types : rotation, nutation and elongated motion.

Without loss of generality, the uniform vorticity ω and the area of the elliptic vortex are fixed to 1 and π, respectively. For given values of γ and s, the motion of the elliptic vortex is obtained by the numerical integration of Eq.(2) with initial conditions $r = r_0$ and $\theta = \theta_0$. In the present paper, we consider only the case of $s \geqq 0$ and $\gamma = 0$. We usually use the initial conditions satisfying $0 < r_0 < 1$ and $\theta_0 = 0$. It is found from Eq.(2) that r is always less than 1 under these conditions.

2.2 Motion of fluid particles around a vortex

The motion of a fluid particle in a two-dimensional flow of an incompressible fluid is governed by

$$\dot{x} = \frac{\partial\Psi}{\partial y}, \qquad \dot{y} = -\frac{\partial\Psi}{\partial x}, \tag{4}$$

where Ψ is a stream function and (x, y) is the location of the particle. Equation (4) can be interpreted as the Hamilton's canonical equation with (generally time-dependent) Hamiltonian Ψ. Therefore, the motion of a fluid particle in the (x, y) plane corresponds to the motion of a representative point in the phase space of a Hamiltonian system with one degree of freedom.

The stream function of the external shear flow is already given in Eq.(1). The stream function of the flow induced by the elliptic vortex is given by

$$\psi_v = -\frac{1}{4}e^{-2\xi}\cos 2\eta - \frac{1}{2}\xi, \tag{5}$$

where (ξ, η) are elliptic coordinates fixed to the vortex. This (ξ, η) is related to Cartesian coordinates (X, Y) by

$$X = k \cosh\xi \cos\eta, \qquad Y = k \sinh\xi \sin\eta, \tag{6}$$

where $k^2 = (1 - r^2)/r$. The X and Y axes rotate with the vortex and correspond to the major and minor axes, respectively. Therefore, relations

$$x = X\cos\theta - Y\sin\theta, \qquad y = X\sin\theta + Y\cos\theta, \tag{7}$$

are satisfied.

Total stream function Ψ is given by

$$\Psi = \psi_e + \psi_v. \tag{8}$$

In the numerical computations of the motion of fluid particles, we use the elliptic coordinates. Using Eqs.(6), (7) and (8), Eq.(4) can be rewritten as

$$\begin{cases} \dot{\xi} &= \dfrac{h^2}{2}\left[-\Omega\sin 2\eta + 2k^{-2}\dfrac{\partial\psi_v}{\partial\eta} + \dfrac{s}{2}\mathcal{F}(\xi,\eta;r,\theta)\right], \\ \dot{\eta} &= \dfrac{h^2}{2}\left[-\Omega\sinh 2\xi - 2k^{-2}\dfrac{\partial\psi_v}{\partial\xi} + \dfrac{s}{2}\mathcal{G}(\xi,\eta;r,\theta)\right], \end{cases} \tag{9}$$

(Polvani & Wisdom 1990), where (ξ, η) is the location of a fluid particle expressed by the elliptic coordinates, and

$$\begin{cases} \Omega = \dfrac{r}{(r+1)^2}, \quad h^2 = (\cosh^2\xi - \cos^2\eta)^{-1}, \\ \mathcal{F} = (\cosh 2\xi \sin 2\eta \cos 2\theta + \sinh 2\xi \cos 2\eta \sin 2\theta) \\ \qquad - \Lambda(\sin 2\eta \cos 2\theta + \sinh 2\xi \sin 2\theta), \\ \mathcal{G} = (\sinh 2\xi \cos 2\eta \cos 2\theta - \cosh 2\xi \sin 2\eta \sin 2\theta) \\ \qquad + \Lambda(\sin 2\eta \sin 2\theta - \sinh 2\xi \cos 2\theta), \\ \Lambda = \dfrac{1+r^2}{1-r^2}. \end{cases} \tag{10}$$

Here the error in the expression of the second term of $\mathcal{G}$ in the paper by Polvani & Wisdom(1990) was corrected. It should be noted that the right-hand side of Eq.(9) explicitly depends on t because r and θ generally change with t as the solution to equations

$$\dot{r} = -sr\sin 2\theta, \qquad \dot{\theta} = \Omega + \frac{1}{2}s\Lambda\cos 2\theta. \tag{11}$$

In the following sections, we examine the motion of fluid particles around the vortex both analytically and numerically using Eqs.(9) and (11). Here we restrict our study to the range of s for which the vortex rotates. It can be shown from Eq.(11) that the vortex rotates if s is less than a certain value under the initial conditions $0 < r_0 < 1$ and $\theta_0 = 0$. For example, this value is 0.173 for $r_0 = 0.5$.

3 Motion of fluid particles in two special flows

3.1 Flow due to the Kirchhoff elliptic vortex

If we assume that $s = 0$ (no external flow) in Eq.(11), we obtain

$$r = r_0, \qquad \theta = \Omega_0 t, \tag{12}$$

where

$$\Omega_0 = \frac{r_0}{(r_0+1)^2}. \tag{13}$$

This vortex which rotates at the constant angular velocity Ω_0 without deformation is well known as the Kirchhoff elliptic vortex. Substituting Eq.(12) into Eq.(9) with $s = 0$, we obtain

$$\begin{cases} \dot{\xi} &= \hat{f}_1(\xi,\eta) \equiv \dfrac{h^2}{2}\left(-\Omega_0 + k_0^{-2}e^{-2\xi}\right)\sin 2\eta, \\ \dot{\eta} &= \hat{f}_2(\xi,\eta) \equiv \dfrac{h^2}{2}\left[-\Omega_0 \sinh 2\xi - k_0^{-2}\left(e^{-2\xi}\cos 2\eta - 1\right)\right], \end{cases} \tag{14}$$

as the equation governing the motion of a fluid particle in the flow due to the Kirchhoff elliptic vortex, where $k_0^2 = (1 - r_0^2)/r_0$.

Equation (14) has two pairs of equilibrium points $(\xi,\eta) = (\bar{\xi},\bar{\eta})$ expressed by

$$\left(\bar{\xi},\bar{\eta}\right) = \left(\bar{\xi_1}^{\pm},\bar{\eta_1}^{\pm}\right) \equiv \left(\frac{1}{2}\log\left[\frac{3r_0+1}{1-r_0}\right], -\frac{\pi}{2} \pm \frac{\pi}{2}\right), \tag{15}$$

and

$$\left(\bar{\xi},\bar{\eta}\right) = \left(\bar{\xi_2}^{\pm},\bar{\eta_2}^{\pm}\right) \equiv \left(\frac{1}{2}\log\left[\frac{3+r_0}{1-r_0}\right], \pm\frac{\pi}{2}\right). \tag{16}$$

The Jacobian matrix J of Eq.(14) at $(\xi,\eta) = (\bar{\xi},\bar{\eta})$ is expressed as

$$J = \bar{h}^2 \begin{pmatrix} -k_0^{-2}e^{-2\bar{\xi}}\sin 2\bar{\eta} & -\Omega_0\cos 2\bar{\eta} + k_0^{-2}e^{-2\bar{\xi}}\cos 2\bar{\eta} \\ -\Omega_0\cosh 2\bar{\xi} + k_0^{-2}e^{-2\bar{\xi}}\cos 2\bar{\eta} & k_0^{-2}e^{-2\bar{\xi}}\sin 2\bar{\eta} \end{pmatrix}, \tag{17}$$

where $\bar{h}^2 = (\cosh^2\bar{\xi} - \cos^2\bar{\eta})^{-1}$.

Substituting Eq.(15) into Eq.(17), we obtain the Jacobian matrix for both equilibrium points $(\bar{\xi_1}^{\pm},\bar{\eta_1}^{\pm})$. The eigenvalues of this matrix are given by

$$\lambda_1^{\pm} = \pm\frac{\sqrt{(1-r_0)(3r_0+1)}}{2(1+r_0)^2},$$

and are real with different signs since $0 < r_0 < 1$. Therefore, these equilibrium points are saddles.

Substituting Eq.(16) into Eq.(17), we obtain the Jacobian matrix for both equilibrium points $(\bar{\xi_2}^{\pm},\bar{\eta_2}^{\pm})$. The eigenvalues of this matrix are given by

$$\lambda_2^{\pm} = \pm\frac{r_0\sqrt{(1-r_0)(3+r_0)}}{2(1+r_0)^2}i. \tag{18}$$

Since $\lambda_2^{\pm}$ are pure imaginary, these equilibrium points are centers.

The motion of fluid particles on the (X, Y) plane fixed to the vortex is shown in Fig.1(a). In this figure, the saddles $(\xi, \eta) = (\bar{\xi_1}^{\pm}, \bar{\eta_1}^{\pm})$ are on the major axis of the elliptic vortex as expressed by A and B, whereas the centers $(\xi, \eta) = (\bar{\xi_2}^{\pm}, \bar{\eta_2}^{\pm})$ are on the minor axis as expressed by C and D. There are also four heteroclinic orbits $H_1^{\pm}$ and $H_2^{\pm}$ connecting these saddles. These equilibrium points and heteroclinic orbits rotate relative to the (x, y) plane fixed to the fluid at infinity. However, if we introduce the Poincaré map of the (x, y) coordinates of the locations of fluid particles after every period of the vortex's rotation (at $t = 2n\pi/\Omega_0$, where n is an integer), these points and orbits are also the fixed points and heteroclinic orbits of this map, respectively.

3.2 Flow in the point-vortex approximation

The velocity of the external shear flow is proportional to s and is larger at the point of larger distance from the origin, whereas the velocity induced by the vortex is smaller at the point of larger distance from the origin. Therefore, if s is small, these velocities are expected to be of the same order in a region appropriately far from the vortex. In the consideration of the flow in a region far from the elliptic vortex, this vortex can be approximated by a point vortex of the same circulation π. The stream function due to a point vortex at the origin with strength π in a linear shear flow expressed by Eq.(1) with $\gamma = 0$ is given by

$$\psi_1 = -\frac{1}{4} sR^2 \cos 2\Theta - \frac{1}{2} \log R, \tag{19}$$

where (R, Θ) are polar coordinates defined by

$$x = R\cos\Theta, \qquad y = R\sin\Theta. \tag{20}$$

Therefore, the evolution of a particle's position (R, Θ) is governed by

$$\dot{R} = \frac{1}{R}\frac{\partial \psi_1}{\partial \Theta} = \frac{1}{2} sR \sin 2\Theta, \qquad \dot{\Theta} = -\frac{1}{R}\frac{\partial \psi_1}{\partial R} = \frac{1}{2} s\cos 2\Theta + \frac{1}{2R^2}. \tag{21}$$

Equation (21) has a pair of equilibrium points expressed by

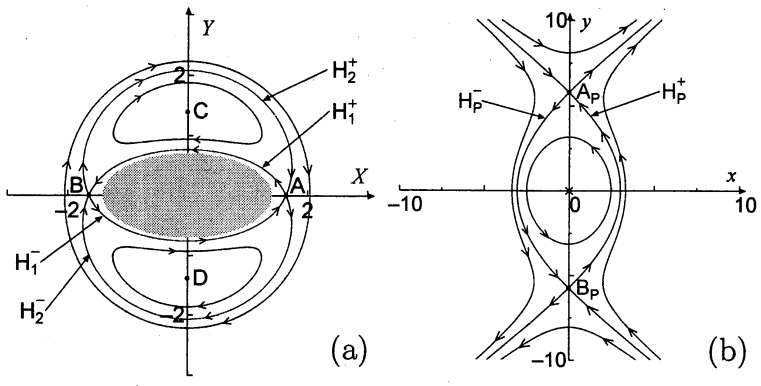

Figure 1: (a)Motion of fluid particles around the Kirchhoff elliptic vortex on the (X, Y) plane fixed to the vortex. $r_0 = 0.5$. (b)Motion of fluid particles in the point-vortex approximation. $s = 0.03$.

$$(R,\Theta)=(R_1^{\pm},\Theta_1^{\pm})\equiv\left(\frac{1}{\sqrt{s}},\pm\frac{\pi}{2}\right). \tag{22}$$

The Jacobian matrix J_2 of Eq.(21) at these points is given by

$$J_2=\begin{pmatrix}\frac{1}{2}s\sin 2\Theta_1^{\pm} & sR_1^{\pm}\cos 2\Theta_1^{\pm}\\ -\frac{1}{R_1^{\pm 3}} & -s\sin 2\Theta_1^{\pm}\end{pmatrix}=\begin{pmatrix}0 & -\sqrt{s}\\ -s\sqrt{s} & 0\end{pmatrix}.$$

The eigenvalues of this matrix are $\pm s$. Since these are real with different signs, the equilibrium points are saddles.

The motion of fluid particles in this flow of the point-vortex approximation is shown in Fig.1(b). Here $\mathrm{A_P}$ and $\mathrm{B_P}$ are saddles given by Eq.(22). There are also a pair of heteroclinic orbits $\mathrm{H_P^{\pm}}$ connecting these saddles. These points and orbits are also the fixed points and heteroclinic orbits of the Poincaré map introduced at the end of the preceding subsection.

4 Melnikov's method applied to the flow for small s

4.1 Melnikov function

We consider a two-dimensional system expressed by

$$\dot{\tilde{x}}=f_1(\tilde{x},\tilde{y})+\varepsilon g_1(\tilde{x},\tilde{y};t),\qquad \dot{\tilde{y}}=f_2(\tilde{x},\tilde{y})+\varepsilon g_2(\tilde{x},\tilde{y};t), \tag{23}$$

where ε is a small parameter. The perturbation terms g_1 and g_2 are assumed to be time-periodic with a period $2\pi/\upsilon$. We also assume that the unperturbed system ((23) with $\varepsilon=0$) has two saddles $\mathrm{P_0^{\pm}}$ and two heteroclinic orbits $\mathrm{H_0^{\pm}}$, expressed by $\tilde{x}=\tilde{x}_0^{\pm}(t)$ and $\tilde{y}=\tilde{y}_0^{\pm}(t)$, connecting them. Therefore,

$$\lim_{t\to\pm\infty}(\tilde{x}_0^{+}(t),\tilde{y}_0^{+}(t))=\mathrm{P_0^{\pm}}\quad\text{and}\quad\lim_{t\to\pm\infty}(\tilde{x}_0^{-}(t),\tilde{y}_0^{-}(t))=\mathrm{P_0^{\mp}}, \tag{24}$$

are satisfied.

Since the right-hand side of Eq.(23) is time-periodic, we can define a two-dimensional map which maps each value of $(\tilde{x},\tilde{y})$ at $t=0$ onto its value at $t=2\pi/\upsilon$. From the above assumptions on the unperturbed system, this map has two saddles $\mathrm{P_\varepsilon^{\pm}}$, near $\mathrm{P_0^{\pm}}$.

Here we introduce the Melnikov functions $M^{\pm}(\phi)$ for the heteroclinic orbits $\mathrm{H_0^{\pm}}$ defined by

$$\begin{aligned}M^{\pm}(\phi) &= \int_{-\infty}^{\infty}\Big\{f_1\left(\tilde{x}_0^{\pm}(t),\tilde{y}_0^{\pm}(t)\right)g_2\left(\tilde{x}_0^{\pm}(t),\tilde{y}_0^{\pm}(t);t+\phi\right)\\ &\qquad -f_2\left(\tilde{x}_0^{\pm}(t),\tilde{y}_0^{\pm}(t)\right)g_1\left(\tilde{x}_0^{\pm}(t),\tilde{y}_0^{\pm}(t);t+\phi\right)\Big\}\,dt,\end{aligned} \tag{25}$$

where ϕ is a phase variable. These functions are periodic with period $2\pi/\upsilon$. The following result is known in the Melnikov theory (e.g. Wiggins 1990) : If there are ϕ_0^{+} and ϕ_0^{-} satisfying

$$M^{+}(\phi_0^{+})=0,\quad \left.\frac{dM^{+}(\phi)}{d\phi}\right|_{\phi=\phi_0^{+}}\neq 0,\qquad M^{-}(\phi_0^{-})=0,\quad \left.\frac{dM^{-}(\phi)}{d\phi}\right|_{\phi=\phi_0^{-}}\neq 0, \tag{26}$$

then for non-zero ε the stable manifold $\mathrm{W_s^{+}[W_s^{-}]}$ of saddle $\mathrm{P_\varepsilon^{+}[P_\varepsilon^{-}]}$ and the unstable manifold $\mathrm{W_u^{-}[W_u^{+}]}$ of saddle $\mathrm{P_\varepsilon^{-}[P_\varepsilon^{+}]}$ intersect transversely. This means that the system (23) has a chaotic dynamics for non-zero ε near the heteroclinic orbits $\mathrm{H_0^{\pm}}$.

4.2 Perturbation from the flow due to the Kirchhoff elliptic vortex

In this subsection, we consider Eqs.(9) and (11) under the assumption of small s. We first expand r and θ with respect to s as

$$r = \hat{r_0} + s\hat{r_1} + s^2\hat{r_2} + \cdots \quad , \quad \theta = \hat{\theta_0} + s\hat{\theta_1} + s^2\hat{\theta_2} + \cdots . \tag{27}$$

Substituting Eq.(27) into Eq.(11), we obtain

$$\hat{r_0} = r_0, \qquad \hat{\theta_0} = \Omega_0 t + \frac{\pi}{4}, \tag{28}$$

from the equations in O(1), under the initial conditions $r = r_0$ and $\theta = \pi/4$ at $t = 0$. Here this initial value of θ was chosen so that the average value of r is still r_0 even if O(s) variation determined below is included. In O(s),

$$\dot{\hat{r_1}} = -\hat{r_0} \sin 2\hat{\theta_0}, \tag{29}$$

is derived. Using Eq.(28) and the initial condition $\hat{r_1} = 0$ at $t = 0$, Eq.(29) is solved to give

$$\hat{r_1} = \frac{(1+r_0)^2}{2} \sin 2\Omega_0 t, \tag{30}$$

Substituting Eq.(27) into Eq.(9), and using Eqs.(28) and (30), we obtain

$$\dot{\xi} = \hat{f_1}(\xi,\eta) + s\hat{g_1}(\xi,\eta;t), \qquad \dot{\eta} = \hat{f_2}(\xi,\eta) + s\hat{g_2}(\xi,\eta;t), \tag{31}$$

after truncating terms of O(s^2), where $\hat{f_1}(\xi,\eta)$ and $\hat{f_2}(\xi,\eta)$ are given in Eq.(14) and

$$\begin{cases} \hat{g_1}(\xi,\eta;t) = \dfrac{h^2}{4}\left[-\dfrac{1-r_0}{1+r_0}\sin 2\eta \sin 2\Omega_0 t \right. \\ \qquad\qquad \left. + \dfrac{1+r_0^2}{(1-r_0)^2} e^{-2\xi} \sin 2\eta \sin 2\Omega_0 t + \mathcal{F}\left(\xi,\eta;r_0,\Omega_0 t + \dfrac{\pi}{4}\right)\right], \\ \hat{g_2}(\xi,\eta;t) = \dfrac{h^2}{4}\left[-\dfrac{1-r_0}{1+r_0}\sinh 2\xi \sin 2\Omega_0 t \right. \\ \qquad\qquad \left. - \dfrac{1+r_0^2}{(1-r_0)^2}(e^{-2\xi}\cos 2\eta - 1)\sin 2\Omega_0 t + \mathcal{G}\left(\xi,\eta;r_0,\Omega_0 t + \dfrac{\pi}{4}\right)\right]. \end{cases} \tag{32}$$

The first and second terms in the expressions of $\hat{g_1}$ and $\hat{g_2}$ come from the expansion of Ω and k included in the first-order terms of Eq.(9) with respect to s. The perturbation terms $\hat{g_1}$ and $\hat{g_2}$ are time-periodic with period π/Ω_0.

As shown in section 3.1, the non-perturbed system (Eq.(31) with $s = 0$) have two pairs of heteroclinic orbits $\mathrm{H}_1^{\pm}$ and $\mathrm{H}_2^{\pm}$. If the motion of a fluid particle on these heteroclinic orbits is expressed by $(\xi_1^{\pm}(t), \eta_1^{\pm}(t))$ and $(\xi_2^{\pm}(t), \eta_2^{\pm}(t))$, the Melnikov functions for these orbits are given by

$$\begin{aligned} M_j^{\pm}(\phi) = \int_{-\infty}^{\infty} \Big\{ & \hat{f_1}\left(\xi_j^{\pm}(t), \eta_j^{\pm}(t)\right) \hat{g_2}\left(\xi_j^{\pm}(t), \eta_j^{\pm}(t); t+\phi\right) \\ & - \hat{f_2}\left(\xi_j^{\pm}(t), \eta_j^{\pm}(t)\right) \hat{g_1}\left(\xi_j^{\pm}(t), \eta_j^{\pm}(t); t+\phi\right) \Big\} dt \quad (j = 1, 2), \end{aligned} \tag{33}$$

These functions are periodic in ϕ with period π/Ω_0. The flow field of Eq.(31) has the symmetry that $\hat{f}_j(\xi, \eta + \pi) = \hat{f}_j(\xi, \eta)$ and $\hat{g}_j(\xi, \eta + \pi; t) = \hat{g}_j(\xi, \eta; t)$ for $j = 1$ and 2. Therefore, if we assume that $(\xi_j^+(0), \eta_j^+(0)) = (\xi_j^-(0), \eta_j^-(0) + \pi)$ then $(\xi_j^+(t), \eta_j^+(t)) = (\xi_j^-(t), \eta_j^-(t) + \pi)$ is satisfied for all t. This yields the relations $M_j^+(\phi) = M_j^-(\phi)$ for $j = 1$ and 2.

Figure 2(a) and (b) shows these Melnikov functions numerically computed for $r_0 = 0.5$. Both of these functions intersect the zero transversely. Therefore, we expect that there exist chaotic dynamics for non-zero s near the heteroclinic orbits $\mathrm{H}_1^{\pm}$ and $\mathrm{H}_2^{\pm}$.

4.3 Perturbation from the flow in the point-vortex approximation

In this subsection, we study the perturbation from the flow in the point-vortex approximation for small s. If we consider the flow due to the elliptic vortex with aspect ratio r and inclination angle θ in the external shear flow, the stream function of this flow in a region far from this vortex is expanded as

$$\psi_2 = -\frac{1}{4} sR^2 \cos 2\Theta - \frac{1}{2} \log R + \frac{k^2}{16R^2} \cos 2(\Theta - \theta) + \mathrm{O}(R^{-4}), \tag{34}$$

where R and Θ are defined by Eq.(20). The terms on the right-hand side of Eq.(34) except for the first one are derived by expanding Eq.(5) for large ξ and using the relations (6), (7) and (20).

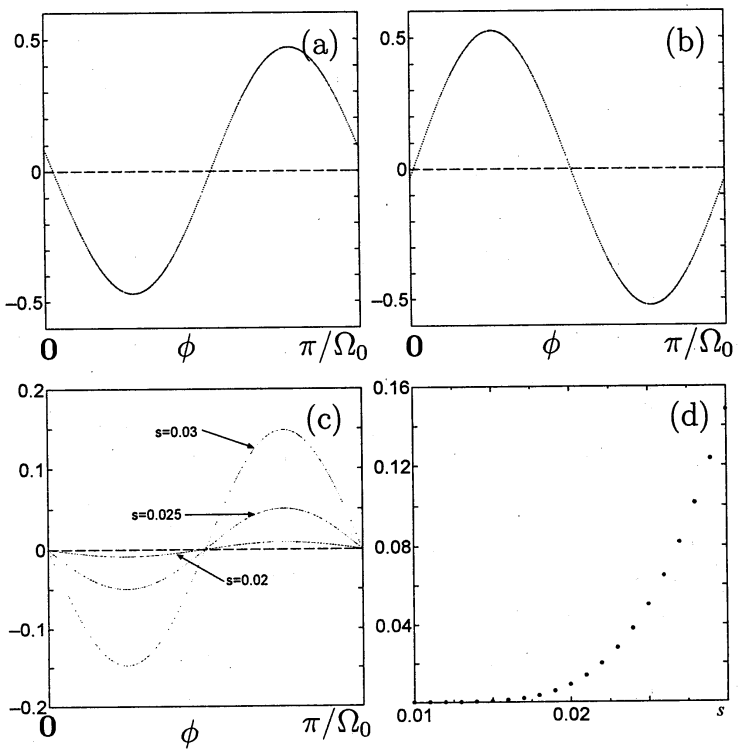

Figure 2: Melnikov functions for $r_0 = 0.5$. (a)$M_1^{\pm}(\phi)$, (b)$M_2^{\pm}(\phi)$. (c)$M_{\mathrm{P}}^{\pm}(\phi; s)$ for a few s. (d)Dependence of the maximum value of $M_{\mathrm{P}}^{\pm}(\phi; s)$ on s.

From Eq.(34), we find that the velocities caused by the external shear and by the vortex are of the same order in a region of distance $O(1/\sqrt{s})$ from the origin. Therefore, we introduce a stretched radial variable $\tilde{R} = \sqrt{s}R$. Using this variable, we obtain

$$\left\{ \begin{array}{rcl} \dfrac{d\tilde{R}}{d\tilde{t}} & = & \dfrac{1}{\tilde{R}}\dfrac{\partial \psi_2}{\partial \Theta} = \tilde{f}_1(\tilde{R},\Theta) + s\tilde{g}_1\left(\tilde{R},\Theta;\dfrac{\tilde{t}}{s}\right), \\ \dfrac{d\Theta}{d\tilde{t}} & = & -\dfrac{1}{\tilde{R}}\dfrac{\partial \psi_2}{\partial \tilde{R}} = \tilde{f}_2(\tilde{R},\Theta) + s\tilde{g}_2\left(\tilde{R},\Theta;\dfrac{\tilde{t}}{s}\right), \end{array} \right. \tag{35}$$

from Eq.(34) after truncating $O(s^2)$ terms, as the equation which governs the evolution of the location $(\tilde{R},\Theta)$ of a fluid particle. Here $\tilde{t} = st$ is the slow time variable, and

$$\left\{ \begin{array}{l} \tilde{f}_1(\tilde{R},\Theta) = \dfrac{1}{2}\tilde{R}\sin 2\Theta, \qquad \tilde{f}_2(\tilde{R},\Theta) = \dfrac{1}{2}\cos 2\Theta + \dfrac{1}{2\tilde{R}^2}, \\ \tilde{g}_1\left(\tilde{R},\Theta;\dfrac{\tilde{t}}{s}\right) = -\dfrac{k_0^2}{8\tilde{R}^3}\sin 2\left(\Theta - \dfrac{\Omega_0}{s}\tilde{t}\right), \\ \tilde{g}_2\left(\tilde{R},\Theta;\dfrac{\tilde{t}}{s}\right) = \dfrac{k_0^2}{8\tilde{R}^4}\cos 2\left(\Theta - \dfrac{\Omega_0}{s}\tilde{t}\right). \end{array} \right. \tag{36}$$

In the derivation of above expressions, since r and θ were included only in the perturbation terms, these variables were replaced by r_0 and $\Omega_0 t$.

As shown in section 3.2, the non-perturbed system (Eq.(35) with $s = 0$) has two heteroclinic orbits $H_P^{\pm}$. If the motion of a fluid particle on these heteroclinic orbits is expressed by $(\tilde{R}_0^{\pm}(t), \Theta_0^{\pm}(t))$, the Melnikov functions for these orbits are given by

$$\begin{aligned} M_P^{\pm}(\phi;s) = \int_{-\infty}^{\infty} \Bigg\{ & \tilde{f}_1\left(\tilde{R}_0^{\pm}(\tilde{t}),\Theta_0^{\pm}(\tilde{t})\right)\tilde{g}_2\left(\tilde{R}_0^{\pm}(\tilde{t}),\Theta_0^{\pm}(\tilde{t});\frac{\tilde{t}}{s}+\phi\right) \\ & - \tilde{f}_2\left(\tilde{R}_0^{\pm}(\tilde{t}),\Theta_0^{\pm}(\tilde{t})\right)\tilde{g}_1\left(\tilde{R}_0^{\pm}(\tilde{t}),\Theta_0^{\pm}(\tilde{t});\frac{\tilde{t}}{s}+\phi\right)\Bigg\} d\tilde{t}, \end{aligned} \tag{37}$$

These functions are periodic in ϕ with period π/Ω_0. The flow field of Eq.(35) has the symmetry that $\tilde{f}_j(\tilde{R},\Theta+\pi) = \tilde{f}_j(\tilde{R},\Theta)$ and $\tilde{g}_j(\tilde{R},\Theta+\pi) = \tilde{g}_j(\tilde{R},\Theta)$ for $j = 1$ and 2. Therefore, if we assume that $(\tilde{R}_0^+(0),\Theta_0^+(0)) = (\tilde{R}_0^-(0),\Theta_0^-(0)+\pi)$, then $(\tilde{R}_0^+(t),\Theta_0^+(t)) = (\tilde{R}_0^-(t),\Theta_0^-(t)+\pi)$ is satisfied for all t. This yields the relation $M_P^+(\phi;s) = M_P^-(\phi;s)$. Here it should be noted that Eq.(35) is different from the standard form cosidered in the Melnikov theory, such as Eq.(23), in that the period of the perturbation terms $\tilde{g}_1$ and $\tilde{g}_2$ depends on the perturbation parameter s. This results in the s-dependence of the functions $M_P^{\pm}$. However, we still call these functions the Melnikov functions because it seems that from the following reason these functions can be used to estimate the distance between the stable and unstable manifolds of the saddles. The functions $M_P^{\pm}$ can be interpreted as a Fourier transform of a function which tends to zero exponentially as $\tilde{t} \to \pm\infty$. Here $2\Omega_0/s$ corresponds to the "frequency" variable. In the theory of the Fourier transform, it is known that the Fourier transform of a rapidly decreasing function tends to zero faster than any minus powers of the "frequency" variable as this variable increases to the infinity. This suggests that as s decreases to zero, $M_P^{\pm}$ tends to zero faster than any powers of s. Furthermore, the higher-order terms in the expansion of ψ_2 have the s-dependence of the form $\cos(2^n\Omega_0\tilde{t}/s)$ $(n = 2,3,4,\ldots)$. Therefore, it seems reasonable to expect that $M_P^{\pm}$ is

the leading-order term in the estimation of the distance between the stable and unstable manifolds of the saddles.

Figure 2(c) shows the Melnikov functions $M_{\mathrm{P}}^{\pm}(\phi; s)$ numerically computed for a few s with $r_0 = 0.5$. Since these functions transversely intersect the zero, we can expect that there exist chaotic dynamics for non-zero s near the heteroclinic orbits $\mathrm{H}_{\mathrm{P}}^{\pm}$. Moreover, the maximum of $|M_{\mathrm{P}}^{\pm}(\phi; s)|$ for all ϕ rapidly decreases to zero with s, as shown in Fig.2(d). This is consistent with the above theoretical prediction.

5 Results of numerical computations

In this section, the motion of fluid particles for several s and r_0 is examined by the numerical integration of Eqs.(9) and (11). Here, we used the Adams-Moulton's predictor-corrector method with variable step size and variable degrees of the prediction and correction formulas. The relative accuracy in the computation was chosen as 3.6×10^{-13}.

5.1 Poincaré plots

In this subsection, the particles' motion is examined using the Poincaré plots of their locations at the times when the major axis of the elliptic vortex agrees with the x axis. We first show the dependence of the motion on s for $r_0 = 0.5$.

Figure 3 shows the Poincaré plots near the vortex for small s. A chaotic region appears as a narrow band region near the heteroclinic orbits $\mathrm{H}_1^{\pm}$ and $\mathrm{H}_2^{\pm}$ introduced in section 3.1, as found from the comparison of Fig.3 with Fig.1(a). This is consistent with the result of the application of the Melnikov's method in section 4.2. Outside this chaotic region, fluid particles move regularly on closed lines in the Poincaré plot. These closed lines are similar to the streamlines in Fig.1(a), and can be interpreted as the KAM tori in a two-dimensional map corresponding to a near-integrable Hamiltonianian system. Furthermore, several small island regions are also observed. For example, in Fig.3(d), we find two pairs of island regions of period 2 surrounded by the chaotic region, and island regions of period 5 near the outermost KAM torus.

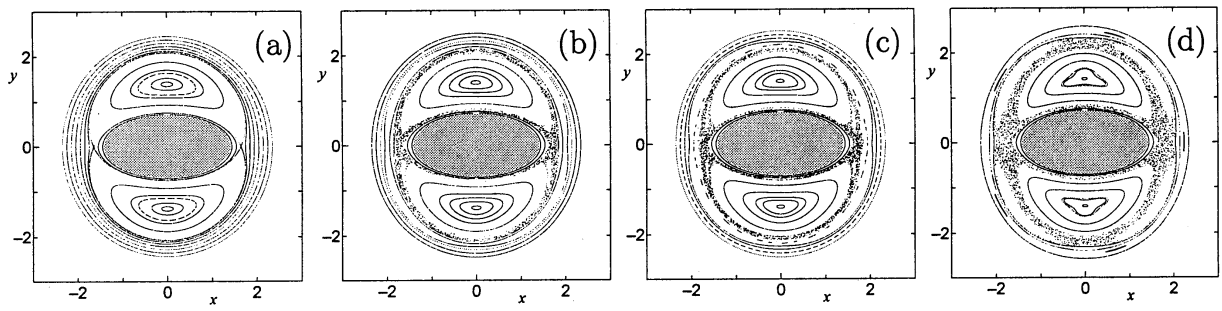

Figure 3: Poincaré plots near the vortex for small s. s is (a)0.00001, (b)0.003, (c)0.005, (d)0.01. Initially, 10 fulid particles are put on the x axis within the range $1.5 \leqq x \leqq 2.5$, and 10 fulid particles are put on the y axis within the ranges $-2.5 \leqq y \leqq -1.5$ and $1.5 \leqq y \leqq 2.5$. The locations of particles in 2500 periods of the vortex's rotation are shown.

Next, the Poincaré plots in the region far from the vortex are shown in Fig.4, where 121 fluid particles are initially put within a small square around the fixed point A_P in Fig.1(b). For small s, these fluid particles move near the heteroclinic orbits $H_P^{\pm}$ introduced in section 3.2. Some particles stay near these heterolinic orbits for a long period, whereas other particles move to the infinity to the upper-right or lower-left direction after a short time. When s is small enough, it is difficult to identify a chaotic motion near $H_P^{\pm}$ from the Poincaré plots (see Fig.4(a)). For larger s, however, we observe a chaotic region near $H_P^{\pm}$. This chaotic region expands rapidly with increasing s, as found from Figs.4(b) and (c).

Figure 4(c) and its magnification Fig.4(d) show a wavy outer boundary of the region where the particles move. This wavy boundary can be interpreted as the result of the transverse intersection of the stable and unstable manifolds of the saddles, near A_P and B_P in Fig.1(b), of the Poincaré map yielded from Eq.(9). That is, in Fig.5, a typical structure of the transversely intersecting stable and unstable manifolds of two saddles P and Q of the Poincaré map of a two-dimensional time-periodic system, called the heteroclinic tangle, is shown. Some of the particles starting near P move toward a region close to Q, where the locations of these particles are bounded by the unstable manifold of Q. Therefore, when

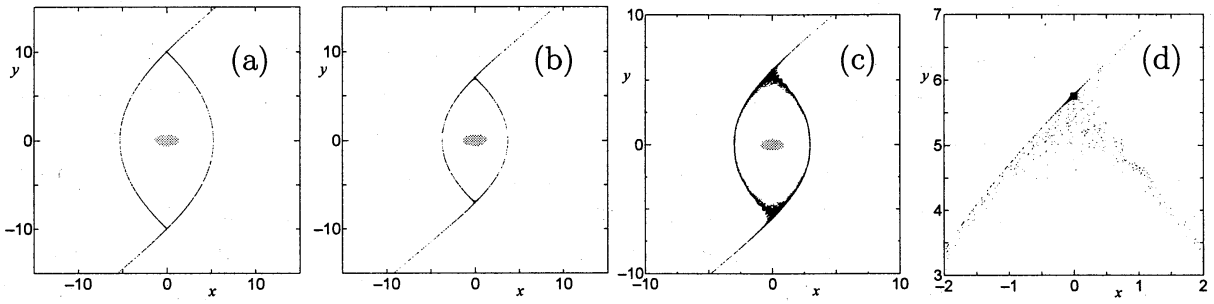

Figure 4: Poincaré plots in the region far from the vortex. s is (a)0.01, (b)0.02, (c)0.03. (d) is the magnification of (c). 11×11 particles are initially put within a square of area 0.01 around the fixed point A_P in Fig.1(b). Locations of particles in 200 periods are plotted.

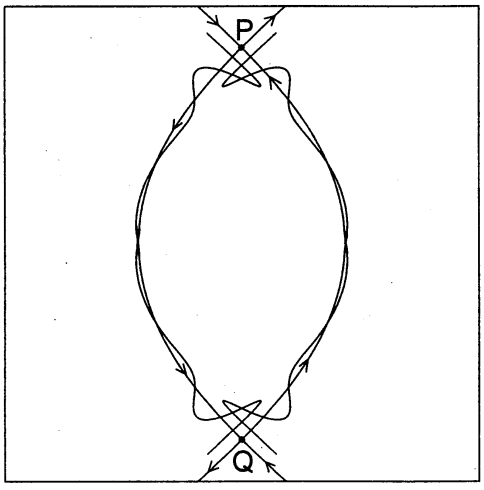

Figure 5: Schematic diagram of the transversely intersecting stable and unstable manifolds of saddles P and Q.

some of these particles return to a region close to P, their locations are still bounded by the unstable manifold of Q, which has a wavy structure near P. From this consideration, it is suggested that the wavy structure in Fig.4(d) expresses the unstable manifold of the saddle near B_P. Furthermore, in Fig.5, since the locations of the particles which return to a region close to P are bounded by the unstable manifold of P, a similar wavy suructure is expected near Q as the manifestation of this unstable manifold. This explains the similar wavy structure in the lower part of Fig.4(c). Therefore, the particles' motion shown in Figs.4(c) and (d) is consistent with the result of the application of the Melnikov theory in section 4.3 which predicts the transverse intersection of the stable and unstable manifolds of the saddles of the Poincaré map.

Figure 6 shows the Poincaré plots both near and far from the vortex for a few s. When s is small, the inner and outer chaotic regions near the heteroclinic orbits $H_1^{\pm}$, $H_2^{\pm}$, and $H_P^{\pm}$ have small widths, and the distance between them is large (of $O(1/\sqrt{s})$). Furthermore, many KAM tori surrounding the vortex and some island regions are observed between these chaotic regions, as illustrated in Fig.6(a). However, as s increases, the widths of these chaotic regions become larger and their distance becomes smaller. Finally, after the disappearance of all the KAM tori surrounding the vortex, these regions merge, as shown in Figure 6. For $r_0 = 0.5$, the KAM tori are observed if $s \leqq 0.028$, as shown in Figs.6(a)-(c). However, we could not find any evidence of the KAM torus in the Poincaré plot for $s = 0.029$, shown in Fig.6(d), even from magnified Poinaré plots for many initial points. We define s_c as the value of s at which this merging occurs. Therefore, s_c is close to 0.029 for $r_0 = 0.5$.

From the theory on the KAM torus in a two-dimensional map, if there exists at least one KAM torus surrounding the vortex, then fluid particles starting near the vortex never move to the infinity. However, when all such KAM tori disappear, these particles may be able to move to the infinity. In our computations, the movement of some fluid particles

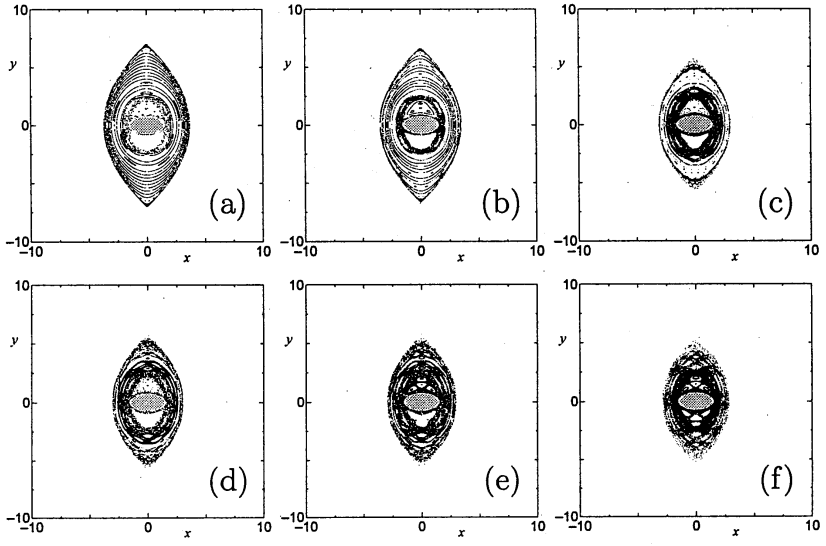

Figure 6: Poincaré plots for $r_0 = 0.5$. s is (a)0.020, (b)0.022, (c)0.028, (d)0.029, (e)0.030, (f)0.032. 21 particles are initially put on the y axis with a constant interval within the range $1.5 \leqq y \leqq 1/\sqrt{s}$. The locations of particles in 5000 periods are shown.

from their initial locations near the vortex to the infinity was observed only for $s \geq 0.031$. For $s = 0.029$ and 0.030, no example of the movement to the infinity was obtained in the computation for 20 initial positions near the vortex for 200000 periods. This discrepancy between the disappearance of the KAM torus and the particle's movement to the infinity may because the particle's motion near the KAM torus which finally disappeared in the direction normal to the torus is quite slow. Polvani & Wisdom(1990) reported that a particle starting near the vortex moves to the infinity for $s = 0.03$. Since they did not give the initial position of this particle definitely, we could not find whether this discrepancy is due to the difference in the numerical schemes used or the difference in the initial positions examined. For s much larger than s_c, most fluid particles starting near the vortex move to the infinity in a short time unless their initial positions are within island regions. However, if s is larger than s_c by only a little amount, most of the particles which finally escape from the vicinity of the vortex move chaotically for a long time near the vortex. Furthermore, the Poincaré plots for such s still have the chaotic regions and island regions of the structure similar to that for $s < s_c$, as illustrated in Fig.6(f).

As found from Figs.3, 4 and 6, for small s, the width of the inner chaotic region is much larger than that of the outer chaotic region.

Next, the dependence of the critical value s_c on the initial aspect ratio r_0 is examined. Figure 7 shows examples of the Poincaré plots for a few r_0. For $r_0 = 0.7$, since the inner and outer chaotic regions do not merge even at $s = 0.035$, as shown in Fig.7(b), s_c is larger than 0.035. On the other hand, s_c for $r_0 = 0.3$ and 0.2 are smaller than 0.025, because the two chaotic regions already merge at this s, as shown in Figs.7(d) and (f). Figure 8 shows the r_0-dependence of s_c determined from the Poincaré plots for several s. The value of s_c is larger for r_0 closer to one. One reason for this r_0-dependence of s_c is the slower growth of the inner chaotic region with increasing s for r_0 closer to one, as illustrated in Figs.6 and 7. These figures also show that the outer chaotic region for the same s is narrower if r_0 is closer

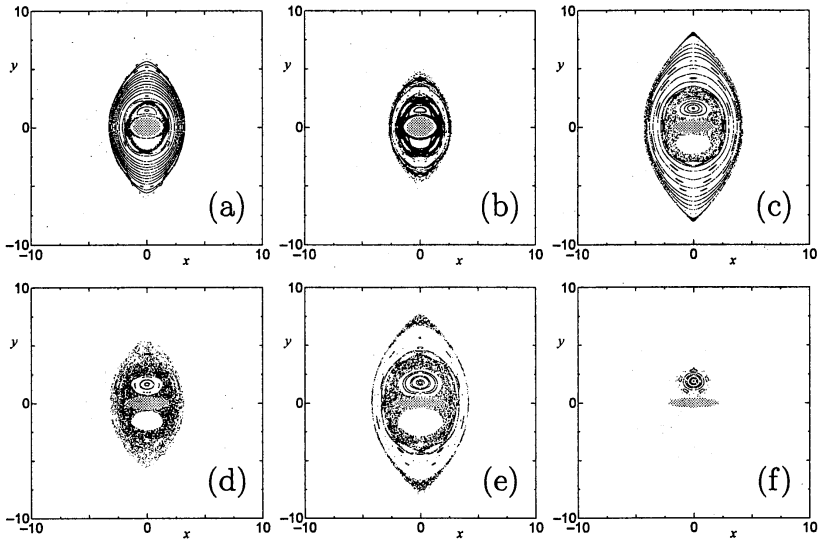

Figure 7: Poincaré plots for a few r_0. r_0 is 0.7 in (a) and (b), 0.3 in (c) and (d), 0.2 in (e) and (f). s is (a)0.025, (b)0.035, (c)0.015, (d)0.025, (e)0.015, (f)0.025. 21 particles are initially put at the same locations as Fig.6. The locations of particles in 5000 periods are shown.

to one. This is because the perturbation from the point-vortex approximation is smaller for r_0 closer to one. Furthermore, heteroclinic orbits $H_P^{\pm}$, whose location is independent of r_0, are more distant from saddles A and B in Fig.1(a) for r_0 closer to one. All these facts suggest the above dependence of s_c on r_0.

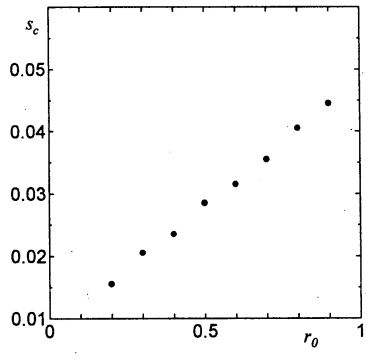

Figure 8: Dependence of s_c on r_0. s_c is determined as the smallest value of s for which no KAM torus can be seen in the Poinaré plot.

References

Dahleh, M.D. (1992) Phys. Fluids, A **4**, 1979-1985

Kida, S. (1981) J. Phys. Soc. Jpn., **50**, 3517-3520

Lamb, H. (1957) Hydrodynamics, 6th edn. Cambridge Univ. Press

Moore, D.W. and Saffman, P.G. (1971) Structure of a line vortex in an imposed strain, in : Aircraft Wake Turbulence and its Detection. Plenum, New York

Polvani, L.M. and Wisdom, J. (1990) Phys. Fluids, A **2**, 123-126

Wiggins, S. (1990) Introduction to Applied Nonlinear Dynamical Systems and Chaos, Springer-Verlag, New York